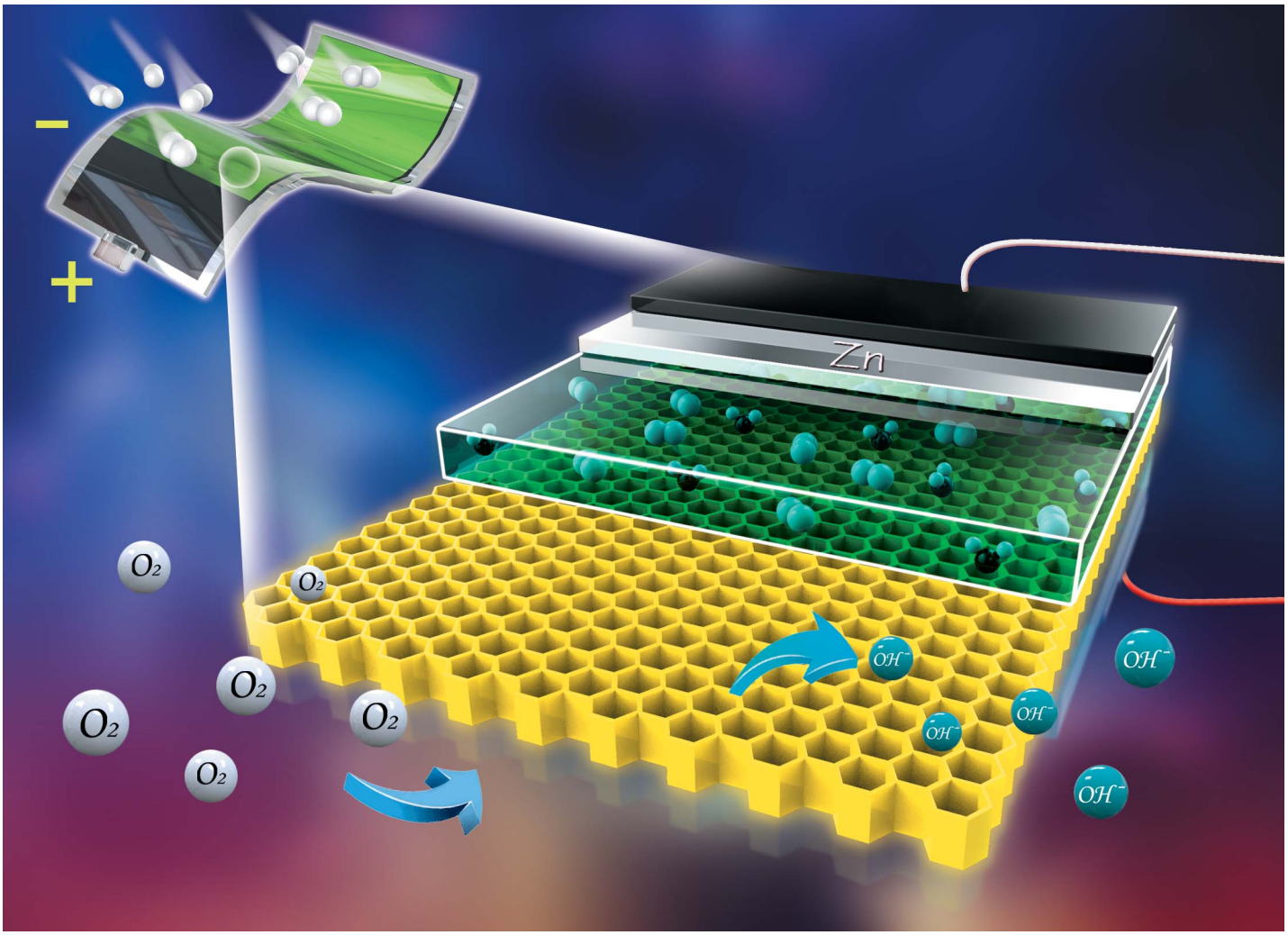

Highlighting research from the laboratory of Prof. Ligui Li and Prof. Shaowei Chen at South China University of Technology.

Volatilizable template-assisted scalable preparation of honeycomb-like porous carbons for efficient oxygen electroreduction

Honeycomb-like nitrogen-doped porous carbons with efficient ORR activity and superb performance in a Zn–air battery were prepared by the pyrolysis of polypyrrole nanosheets containing plenty of volatilizable $FeCl_3$ derivatives, which were facilely prepared *via* an interfacially confined polymerization method.

As featured in:

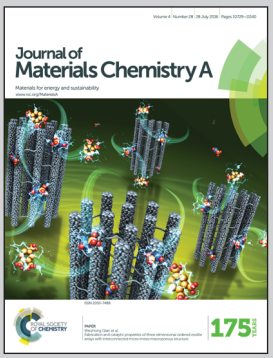

See Ligui Li, Shaowei Chen *et al.*, *J. Mater. Chem. A*, 2016, 4, 10820.

ROYAL SOCIETY OF CHEMISTRY

www.rsc.org/MaterialsA

Registered charity number: 207890

Journal of Materials Chemistry A

PAPER

View Article Online
View Journal | View Issue

Cite this: J. Mater. Chem. A, 2016, 4, 10820

Volatilizable template-assisted scalable preparation of honeycomb-like porous carbons for efficient oxygen electroreduction†

Wenhan Niu,[a] Ligui Li,*[ab] Nan Wang,[a] Shuaibo Zeng,[a] Ji Liu,[a] Dengke Zhao[a] and Shaowei Chen*[ac]

The electrocatalytic activity of nitrogen-doped carbons towards the oxygen reduction reaction is largely determined by the concentration of active nitrogen dopants and the electrochemically accessible surface area. Herein we report a novel, facile route for the preparation of N-doped carbons based on direct pyrolysis of polypyrrole nanosheet precursors synthesized by confining the polymerization on the surface of NaCl crystals using $FeCl_3$ as both the initiator and dopant. In the heating-up process of pyrolysis, a large amount of homogeneously distributed $FeCl_3$ dopant and its derivatives gradually evolved into volatile nanoparticles which helped to generate abundant hierarchical macro- and meso-pores, resulting in honeycomb-like porous carbons with a high content of nitrogen dopants ranging from 7 to 18 at%, a large surface area, and an ORR activity superior to that of commercial Pt/C in alkaline electrolytes. Significantly, by using the best sample that was prepared at 800 °C (HPC-800) as the air electrode, a Zn–air battery was found to display a specific capacity of 647 mA h g^{-1} at 10 mA cm^{-2} and a negligible loss of voltage even after continuous operation for 110 h, a performance markedly better than that with Pt/C as the air cathode. The results not only highlight the significance of precursor engineering in the synthesis of highly efficient nitrogen-doped carbon catalysts for oxygen electroreduction, but also suggest the high potential of the interfacially confined polymerization method in the scalable preparation of cost-effective, highly porous carbons for electrochemical energy storage and conversion devices.

Received 29th April 2016
Accepted 12th May 2016

DOI: 10.1039/c6ta03570a

www.rsc.org/MaterialsA

Introduction

The oxygen reduction reaction (ORR) represents an essential process at the cathodes of fuel cells and metal-air batteries. Because of its complicated reaction pathways and sluggish electron-transfer kinetics, the ORR has been recognized as a major bottleneck that largely determines the device efficiency, and hence the development and utilization of efficient electrocatalysts is crucial for the implementation of these technologies.[1–41] Platinum-based noble metal nanoparticles have been the catalysts of choice because of their effective catalytic activity for the ORR.[5–7] Yet their drawbacks are apparent, such as high costs, poor tolerance against fuel crossover/CO poisoning and low stability, which impede the wide-spread applications of both fuel cell and metal-air battery technologies.[8–10] Within this context, extensive research efforts have been devoted to the development of non-precious metal catalysts (NPMCs), in particular, heteroatom-doped (*e.g.*, nitrogen, phosphorus, sulfur, *etc.*) carbon catalysts for the ORR.[11–23] Of these, nitrogen-doped carbons are of special interest due to their remarkable ORR activity and unique advantages, such as high conductivity, chemical inertness, and ready availability of various carbonaceous source materials and have been deemed as a promising, viable alternative to Pt for ORR electrocatalysis.

Normally, the ORR activity of nitrogen-doped carbons is largely determined by two factors: (1) the chemical nature of the active sites, *i.e.*, the type of nitrogen dopant and its concentration and (2) the accessibility of active sites that control the mass transport properties and is related to the specific surface area and porous texture.[24] Generally, a high content of active nitrogen dopants in the carbon catalysts is necessary to ensure an apparent ORR activity; yet it remains challenging to control the synthesis of selected nitrogen dopants that are preferred for the ORR by simple pyrolysis of nitrogen-containing precursors. Furthermore, improving the specific surface area of carbons by implanting a large number of hierarchical pores, which serve as mass transfer channels for ORR-relevant species such as H^+,

[a]New Energy Research Institute, College of Environment and Energy, South China University of Technology, Guangzhou 510006, China. E-mail: esguili@scut.edu.cn

[b]Guangdong Provincial Key Laboratory of Atmospheric Environment and Pollution Control, College of Environment and Energy, South China University of Technology, Guangzhou 510006, China

[c]Department of Chemistry and Biochemistry, University of California, 1156 High Street, Santa Cruz, California 95064, USA. E-mail: shaowei@ucsc.edu

† Electronic supplementary information (ESI) available. See DOI: 10.1039/c6ta03570a

OH^-, O_2, H_2O, *etc.*, is another effective way to enhance the ORR activity of carbon catalysts. Preformed foreign template-assisted synthesis is a versatile and robust method which has been used extensively to prepare carbon catalysts with controllable pore structures.[25–27] Yet, it generally entails multiple time- and energy-consuming steps, such as the preparation of nanostructured templates (*e.g.*, porous Al_2O_3, SiO_2, ZnO or their monodisperse nanoparticles), homogenous template implantation, and harsh etching process, which make it difficult for mass production. Moreover, the ORR activity may be compromised because partially active components are inevitably removed in the post-synthesis removal of excess templates through rigorous acidic/basic etching.

Alternatively, we developed a thermally removable nanoparticle template method for the preparation of N-doped mesoporous carbons, where the nanoscale templates were *in situ* formed in the polymer nanosheet precursors and effectively removed during controlled pyrolysis of the polymer matrices, which generated abundant hierarchical pores for efficient ORR electrocatalysis.[28,29] The critical point for enabling this method is to form nanosheet precursors embedded with a high concentration of volatilizable nanocrystal templates. This is non-trivial, as typically the loading of nanoscale templates in polymer nanofibers and nanoparticles is rather limited. Furthermore, in hydrothermal preparation of N-containing polymer nanosheets, reaction vessels that can withstand high pressures and high temperatures are needed, and the process is difficult to scale up. Therefore, within the context of template-assisted synthesis, it remains a challenge to develop facile methods for the preparation of high-performance porous carbon-based ORR catalysts which do not involve the solvo- or hydrothermal process and are viable for mass production.

Herein, we report a novel route for the rational design and readily scalable fabrication of nitrogen-doped honeycomb-like porous carbons (HPCs) with abundant hierarchical macro- and meso-pores by direct pyrolysis of polypyrrole nanosheets doped with $FeCl_3$ that were prepared by an interfacially confined polymerization process. The homogeneously distributed $FeCl_3$ and its derivatives not only helped to generate multi-hierarchical pores in the carbonized polymer matrix during pyrolysis, but also facilitated the formation of catalytically active sites such as pyridinic nitrogens and FeN_x/C moieties in the carbon skeletons. The resulting honeycomb-like porous carbons could realize a high specific surface area of 796.8 $m^2\ g^{-1}$, along with a significant concentration of nitrogen dopants ranging from 7 to 18 at%, which contributed to a remarkable ORR activity in alkaline electrolytes. Electrochemical measurements showed that the ORR catalyst prepared at 800 °C was the best one, which featured a half-wave potential that was 40 mV more positive than that of state-of-the-art commercial Pt/C catalysts, along with a higher diffusion-limited current, an electron-transfer number larger than 3.95 even at low overpotentials, substantially longer durability and stronger poison resistance. Furthermore, by using the obtained honeycomb-like carbons as the air cathode, a Zn–air battery was fabricated which even outperformed that based on commercial Pt/C. These results highlight the significance of $FeCl_3$ dopants in the preparation and engineering of N-doped porous carbons that may be a viable alternative to Pt-based noble metal nanocatalysts in important electrochemical devices, such as metal–air batteries, alkaline fuel cells and chlor-alkali electrolyzers.

Experimental section

Sample preparation

The procedure is summarized in Scheme 1. In a typical synthesis, 5 mL of pyrrole (99.98%) and 1 g of polyvinyl pyrrolidone (PVP-K30) were mixed in 60 mL of ethanol; then 20.0 g of NaCl crystals were added into the above mixture under stirring and dried at 70 °C. After complete evaporation of ethanol, the color of the NaCl crystals changed from white to brown, suggesting that pyrrole and PVP had been successfully deposited on the surface of the NaCl crystals. Then, about 20 mL of a 0.85 M $FeCl_3$ solution was added dropwise to the solid NaCl mixture under mechanical stirring on a hotplate at 120 °C within 3 min to avoid the dissolution of NaCl crystals, and the color of the NaCl crystals was found to change from brown to dark green, suggesting the formation of polypyrrole (PPyNSs–NaCl). The sample was then transferred to a beaker where copious amounts of deionized water were added to dissolve the NaCl crystals. The insoluble components were collected and dried after repeated washing with deionized water, affording purified polypyrrole nanosheets (PPyNSs), which were then pyrolyzed at controlled temperatures (300, 500, 700, 800, or 900 °C) for 2 h in a N_2 atmosphere at a gas flow rate of 300 sccm, resulting in the formation of N-doped honeycomb-like carbons, which were referred to as HPC-*T* with *T* being the calcination temperature.

Two other control samples were also prepared in a similar fashion. In the first experiment, no PVP was added, and only a mixture of polypyrrole nanospheres/nanosheets (PPySp/Sh, Fig. S1†) was obtained. The resulting porous carbons by pyrolysis at 800 °C were referred to as PC(Sp/Sh)-800. In the second experiment, polypyrrole nanofibers (PPyNFs, Fig. S1†) were used instead, which were synthesized by dissolving 0.1 mol of pyrrole monomers in 24 mL of a 1 M HCl solution, followed by the dropwise addition of 200 mL of a 1 M $FeCl_3$ solution under stirring. The resulting polypyrrole nanofibers were then collected from the bottom of the glass container, washed with deionized water, and carbonized at 800 °C for 2 h in a N_2 atmosphere, affording PC(NF)-800.

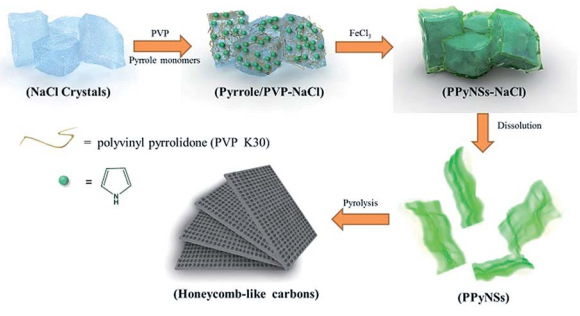

Scheme 1 Schematic illustration of the preparation of nitrogen doped honeycomb-like porous carbons.

Characterization

Transmission electron microscopy (TEM) measurements were conducted on a Tecnai G2-F20 equipped with an EDS detector at an acceleration voltage of 100 kV. The TEM samples were prepared by drop casting a catalyst dispersion directly onto a copper grid coated with a holey carbon film. X-ray photoelectron spectroscopy (XPS) measurements were performed on a Phi X-tool instrument. Powder X-ray diffraction (XRD) patterns were recorded with a Bruker D8-Advance diffractometer using Cu Kα radiation. Thermogravimetric analysis (TGA) was performed on a METTLER instrument under a N_2 atmosphere at a heating rate of 5 °C min^{-1}. The Brunauer–Emmett–Teller (BET) surface area was determined by using a Micromeritics ASAP 2010 with nitrogen adsorption at 77 K using the Barrett–Joyner–Halenda (BJH) method. Raman spectra were recorded on a RENISHAW inVia instrument with an Ar laser source of 488 nm in a macroscopic configuration.

Electrochemistry

All electrochemical measurements were performed with a CHI 750E electrochemical workstation (CH Instruments, Chenhua Co., China) in a conventional three-electrode cell, with a platinum wire as the counter electrode, Ag/AgCl as the reference electrode, and a catalyst-modified glassy carbon electrode (GCE) as the working electrode. The catalyst ink was prepared by adding 1 mg of a catalyst into a solution containing water, isopropanol and Nafion (5%) at a volume ratio of 4 : 1 : 0.025 to form a homogeneous suspension at a catalyst concentration of 1 mg mL^{-1}. A calculated amount (80 μL) of the suspension was then evenly cast on the clean GCE surface with a syringe and dried in air, corresponding to a catalyst loading of 0.4 mg cm^{-2}. The loading of the Pt/C electrode was determined to be 0.2 mg cm^{-2}. Linear sweep voltammograms (LSVs) were acquired in an O_2-saturated 0.1 M KOH aqueous solution at various rotation speeds (400 to 2025 rpm).

The Ag/AgCl reference electrode was calibrated with respect to a reversible hydrogen electrode (RHE). The calibration was performed in a high-purity H_2 (99.999%) saturated electrolyte with two Pt wires as the working and counter electrode, respectively. Cyclic voltammograms were acquired at a low scan rate of 1 mV s^{-1}, and the average of the two potentials at which the current crossed zero was taken as the thermodynamic potential for the hydrogen electrode reactions. In 0.1 M KOH, $E_{RHE} = E_{Ag/AgCl} + 0.975$ V.

The number of electrons transferred (n) during the ORR was calculated by using the following equation (eqn (1))

$$n = \frac{4I_{Disk}}{I_{Ring}/N + I_{Disk}} \quad (1)$$

and the corresponding H_2O_2 yield was evaluated by eqn (2),

$$H_2O_2\% = \frac{200I_{Ring}/N}{I_{Ring}/N + I_{Disk}} \quad (2)$$

where N is the collection efficiency (37%) and I_{Disk} and I_{Ring} are the voltammetric currents at the disk and ring electrodes, respectively.

Zn–air batteries were tested in a home-built electrochemical cell, where the catalysts were loaded on the gas diffusion layer (area of the Teflon-coated carbon fiber paper was 1.0 cm^2, and the catalyst loading was 2.0 mg for all carbon materials and 1.0 mg for Pt/C) as the air cathode and a Zn foil as the anode in 6.0 M KOH. Measurements were carried out on the as-fabricated cell at room temperature with a LAND CT2001A instrument.

Results and discussion

Polymerization of pyrrole or aniline in solution by chemical oxidation usually results in the formation of zero- or one-dimensional polymers. Yet, as depicted in Scheme 1, sheet-like polymers can be readily obtained by confining the polymerization process on a (flat) substrate surface. In addition, the incorporation of PVP is necessary for the synthesis of quasi two-dimensional polymer sheets, where the pyrrole monomers were likely anchored on the dangling ketone groups of PVP by hydrogen bonding (Fig. S2†); without NaCl crystals, only a fiber-like morphology was observed in Fig. S1a,† while without the presence of PVP, a mixture of nanospheres and nanosheets was obtained instead (Fig. S1b†). Furthermore, when $FeCl_3$ was replaced with commonly used ammonium persulfate ($(NH_4)_2S_2O_8$), two-dimensional polypyrrole nanosheets were also obtained (Fig. S3†). These observations clearly demonstrate that the interfacially confined polymerization route presented herein may be exploited as a versatile and robust method for the preparation of two-dimensional polymer sheets.

The formation of polypyrrole nanosheets (PPyNSs) by interfacially confined polymerization was indeed confirmed by TEM measurements, as shown in Fig. 1a, where C, N, Cl and Fe elements can be found to be evenly distributed within the samples by selected area elemental mapping (Fig. 1d). Notably, the Fe-containing compounds in PPyNSs were amorphous as the XRD patterns exhibited only two broad peaks at $2\theta = 11.4$ and 22.3° that arose from polypyrrole (Fig. S4†).[30–32] After high-temperature pyrolysis, the polymer sheets were converted to

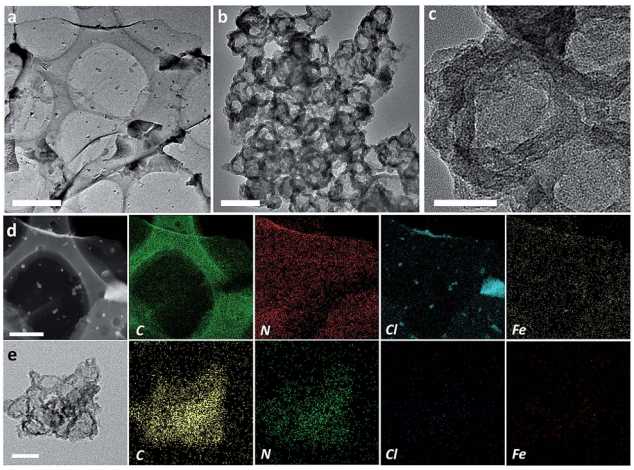

Fig. 1 Representative TEM images and selected-area EDS elemental mapping images of (a and d) PPyNSs and (b, c, and e) HPC-800. Scale bars are (a) 2 μm, (b) 200 nm, (c) 50 nm, (d) 200 nm and (e) 100 nm.

nitrogen-doped carbons (Scheme 1). Fig. 1b and c show the TEM images of the sample prepared by pyrolysis at 800 °C for 2 h (HPC-800), where one can see that the resultant N-doped carbons mainly retained a sheet-like morphology that was markedly wrinkled with a large number of macropores with inner diameters of 50–100 nm (Fig. S5†), resembling the honeycomb structure. From the corresponding elemental maps (Fig. 1e), one can see that high contents of C and N are distributed rather evenly within the sample; however, the signals of Cl and Fe were hardly detectable, which indicated that the polymer sheets were effectively carbonized and Fe moieties had been mostly removed, leaving behind a large number of pores. In fact, the specific surface area of the as-prepared HPC-800 was determined to be 796.8 $m^2 g^{-1}$ based on a type-IV N_2 adsorption/desorption isotherm (Fig. S6a†). Furthermore, the pore size distribution plot confirmed the presence of a hierarchical porous structure with macro- and meso-pores in the range of 3.5–100 nm in diameter (Fig. S6b†), where the mesopores were likely located at the walls of well-defined macropores (Fig. 1c).

Interestingly, when $NH_4S_2O_8$ was used instead of $FeCl_3$ to prepare polypyrrole nanosheets (Fig. S3†), no pores were formed in the carbon sheets after pyrolysis of the polymers at 800 °C, implying that Fe and Cl containing compounds played a vital role in the formation of honeycomb-like structures. To gain further insights into the mechanism of pore formation in the honeycomb-like porous carbons, two other samples (HPC-300 and HPC-500) pyrolyzed at relatively low temperatures were also prepared in a similar fashion. Unlike PPyNSs in which no particulate features were visually observed in the TEM image (Fig. S7a†), the HPC-300 sample showed numerous nanoparticles with diameters less than 10 nm (Fig. S7b†), whereas some agglomerates of nanoparticles were found embedded in the polymer matrix of the HPC-500 sample (Fig. S7c†). Because no diffraction peaks of related Fe-containing compounds were observed, these nanoparticles likely consisted of poorly crystalline iron-containing compounds (Fig. S8†), which acted as rigid templates in the polymer matrix during high-temperature carbonization. As shown in TGA measurements (Fig. S9†), one can see three major weight-loss steps in a N_2 atmosphere. The sudden weight loss of *ca.* 63% starting at about 366 °C was likely due to the formation of a large quantity of volatile compounds such as CO, CO_2, $FeCl_2$, and $FeCl_3$, arising from the decomposition of the polymers and the evaporation of Fe-containing species, which helped to produce a number of cavities/holes in the carbon matrix.[28,33–35] This was supported by XPS analysis in Fig. S10,† where one can see that the Cl2p and Fe2p peaks were clearly defined in the polymer precursor, whereas pyrolysis treatments at elevated temperatures (700, 800, and 900 °C) led to almost complete disappearance of these two elements.

The catalytic activity of the obtained honeycomb-like porous carbons towards the ORR was then evaluated and compared within the context of pyrolysis temperature. As shown in Fig. 2a, rotating disk electrode (RDE) voltammograms showed that the HPC-800 sample exhibited a remarkable onset potential of +1.00 V (*vs.* RHE), markedly more positive than those of the HPCs prepared at other temperatures (+0.81 V for HPC-700,

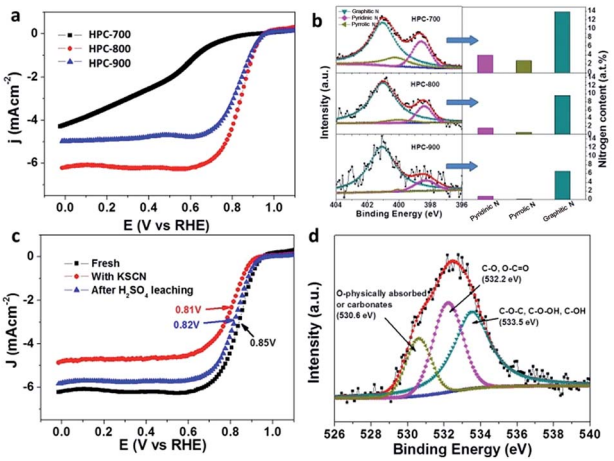

Fig. 2 (a) RDE voltammograms, (b) high-resolution XPS spectra of N1s where black dotted curves are experimental data and colored curves are deconvolution fits (left panels), and the concentrations of various nitrogen dopants in HPC-*T* (*T* = 700, 800 and 900) (right panels). (c) LSV curves of HPC-800 before (black curve) and after H_2SO_4 (blue curve) leaching treatments, and in 0.1 M KOH aqueous solution with the addition of 10 mM KSCN (red curve). All measurements were conducted at a catalyst loading of 0.4 mg cm^{-2} in an O_2-saturated 0.1 M KOH aqueous solution at a sweep rate of 10 mV s^{-1}. (d) XPS spectra of O1s electrons for HPC-800, where the black curve experimental data and colored curves are deconvolution fits. The RDE rotation rate in (a) and (c) was 1600 rpm.

and +0.98 V for HPC-900). In addition, the limiting current density of HPC-800 was also much higher than that of HPC-700 and HPC-900. These results show that the HPC-800 sample represented the best catalyst among the series.

The chemical compositions of the HPC catalysts were then analyzed by XPS measurements. In Fig. 2b, the high-resolution N1s deconvoluted spectrum yielded three pronounced peaks at 398.5, 400.2, and 401.0 eV, which may be ascribed to the pyridinic N, pyrrolic N and graphitic N, respectively.[36,37] One can see that with increasing pyrolysis temperature, the amount of pyrrolic N decreased rapidly, as compared to those of graphitic N and pyridinic N, signifying low stability of pyrrolic N at elevated temperatures. Note that, thanks to the lone-pair electrons, pyridinic N may coordinate with Fe to form Fe–N–C species that have been proposed as active sites for the ORR.[38,39] Graphitic N dopants can also facilitate the adsorption of oxygen molecules on adjacent carbon atoms, which is the rate determining step in the ORR.[13,40,41] Based on the integrated peak areas, one can see that the combined concentration of pyridinic and graphitic N actually decreased with increasing pyrolysis temperature, 17.7 at% for HPC-700, 11.5 at% for HPC-800, and 7.2 at% for HPC-900 (Table S1 and Fig. S11†). The fact that the ORR activity was the lowest with the HPC-700 sample is most likely due to the low porosity, as evidenced by its smallest electrochemical surface area, in comparison with HPC-800 and HPC-900.

In addition, the degree of graphitization of the porous carbons was also examined, as a higher degree of graphitization may lead to higher electrical conductivity and hydrophobicity

which likely helps to increase the ORR activity.[42] From Fig. S12,† it can be seen that the center peak at 284.6 eV of the Csp^2 spectra became increasingly symmetrical with increasing pyrolysis temperature, implying an increasing degree of graphitization of the resulting samples. This is also consistent with the results obtained in XRD (Fig. S13†) and Raman (Fig. S14†) measurements. Moreover, electrochemical impedance spectroscopy (EIS) analysis (Fig. S15†) further confirmed an increase of the electrical conductivity of the porous carbons with increasing pyrolysis temperature. Therefore, the remarkable ORR activity of the HPC-800 catalyst may be ascribed to the combined contributions of a high content of active nitrogen dopants and a high degree of graphitization.[42]

A trace amount of iron species was actually found in the HPC catalysts from high resolution XPS and EDS elemental mapping measurements (0.2 to 0.6 at%, Table S1†). However, the chemical states of the iron moieties remained unclear due to the low concentrations.[43] Although the remarkable ORR activity of Fe, N-codoped carbons has been well documented, some argue that Fe only helps to form active sites and does not directly involve in the ORR catalysis.[44–46] Therefore, it is necessary to identify the actual active sites in HPC-*T* catalysts with trace amounts of iron. Accordingly, two active site-probing experiments were carried out. As shown in Fig. 2c, poisoning the Fe-containing sites with 10 mM KSCN caused a remarkable negative shift of 40 mV in the half-wave potential of the HPC-800 electrode, along with *ca.* 20% decrease of the limiting current density. These results suggested that the Fe-containing compounds likely participate in the catalytic process of the ORR. In contrast, removal of the unstable iron compounds *via* soaking in a hot solution of 1.0 M H_2SO_4 for 6 h caused a small negative shift of the half-wave potential by 30 mV, as compared to the original electrode. Additionally, the O1s electrons of iron oxides (such as Fe_2O_3 and Fe_3O_4) are anticipated to appear at 529.5 eV; yet no such feature was observed in experimental measurements (Fig. 2d);[42,47] no $Fe^{II/III}$ redox couple was detected in voltammetric measurements either, as only featureless voltammograms were obtained in the ORR testing region (0 to +1.1 V *vs.* RHE) even at a high scan rate of 100 mV s^{-1} (Fig. S16†).[48] Taken together, the above results unambiguously demonstrate that the Fe-containing species (*e.g.*, FeN_x moieties) participate in the ORR and hence contribute to partial ORR activity in the present study, as proposed in various recent studies.[49–51] Therefore, the ORR activity of HPC-800 originated predominantly from the synergetic effects between its rich nitrogen dopants, primarily the graphitic and pyridinic nitrogen, and high electrical conductivity. Meanwhile, the abundant macro- and mesoporous structures further enhance the mass transfer process, consequently contributing to an efficient ORR catalyst.

To identify the contributions of macro- and mesopores in HPC-800 to the ORR activity, two additional samples derived from polypyrrole of different morphologies (PC(NF)-800 and PC(Sp/Sh)-800) were prepared and their ORR activity was evaluated for comparison. As depicted in Fig. S17,† no distinct peaks were observed in all the HPC-*T* samples in N_2-saturated electrolyte solution between −0.04 V and +1.16 V, whereas in O_2-saturated 0.1 M KOH, a remarkable oxygen reduction peak was observed at +0.81 V in HPC-800, which is much more positive than that of PC(NF)-800 (+0.51 V) and PC(Sp/Sh)-800 (+0.58 V) at the same loading, and equal to that of commercial Pt/C (20 wt%, 0.2 mg cm^{-2}). Note that the HPC-800 modified electrode exhibited a much larger electrochemical surface area than the two other carbon catalysts based on the integrated area of the electrical double-layer charging curve, signifying that mass transfer in HPC-800 was more efficient because of the formation of macro/mesopores. These results were consistent with the BET surface areas of these samples (Fig. S6, S18, and S19†).

The high electrocatalytic activity of HPC-800 was also manifested in RDE voltammetric measurements. As shown in Fig. 3a, the HPC-800 electrode exhibited a half-wave potential of +0.85 V, more positive than those of Pt/C (+0.81 V), PC(NF)-800 (+0.67 V) and PC(Sp/Sh)-800 (+0.68 V). Concurrently, the current density at +0.80 V was the highest among the series at 4.20 mA cm^{-2} for HPC-800, as compared to 2.89 mA cm^{-2} for Pt/C, 0.36 mA cm^{-2} for PC(NF)-800 and 0.74 mA cm^{-2} for PC(Sp/Sh)-800. In addition, the HPC-800 electrode also exhibited higher electrical conductivity than the two other electrodes (Fig. S20†) as a result of the formation of multiple hierarchical pore structures in HPC-800 that allowed for facile mass transfer of ORR relevant species and ready accessibility to the N-doped active sites. Significantly, the ORR activity of HPC-800 is also close to that of Pt/C in an acid medium (0.1 M $HClO_4$ electrolyte), as shown in Fig. S21,† with a half-wave potential only 59 mV more negative. In fact, the ORR activity of HPC-800 was even better than, or at least comparable to leading results of nitrogen doped carbons and M–N/C catalysts reported in recent studies (Table S2†).[39,52–55]

The ORR kinetics of all samples were explored by using rotating ring-disk electrode (RRDE) measurements. The number of electrons transferred (n) was calculated by using the disk and ring current data, according to eqn (1). As depicted in Fig. 3b, one can see that the n values of HPC-800 were almost 4 in a wide potential range from 0 V to +1.0 V, indicating that

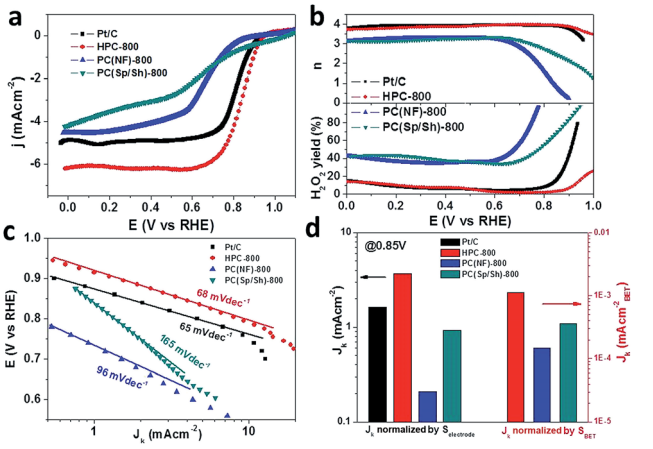

Fig. 3 (a) RDE voltammograms, (b) plots of H_2O_2 yield and number of electrons transferred (n), (c) Tafel plots and (d) comparison of kinetic current densities of a glassy-carbon electrode modified with 0.4 mg cm^{-2} of HPC-800, PC(NF)-800, PC(Sp/Sh)-800 and 0.2 mg cm^{-2} of Pt/C in O_2-saturated 0.1 M KOH solution at a rotation speed of 1600 rpm. The potential sweep rate was 10 mV s^{-1}.

HPC-800 has a high selectivity towards $4e^-$ reduction of oxygen. For instance, the *n* value of HPC-800 was calculated to be 3.96 at +0.60 V, which was slightly higher than that of Pt/C (3.94) but much higher than that of PC(NF)-800 (3.25) and PC(Sp/Sh)-800 (3.32). Additionally, the H_2O_2 yield, calculated according to eqn (2), was as low as 2.46% for the HPC-800 modified electrode at +0.60 V, while it was found to be 4.36% for Pt/C, and even 37.4% for PC(NF)-800 and 34.18% for PC(Sp/Sh)-800 at the same potential. These results further confirm that the HPC-800 behaved as a highly efficient electrocatalyst for the ORR.

For the RDE voltammograms of HPC-800 shown in Fig. S17,† the current density concurrently increased with increasing the electrode rotation speed. In the corresponding Koutecky–Levich (K–L) plots (Fig. S17†), linear fittings with rather comparable slope values were observed for HPC-800 within the potential range of +0.50 to +0.70 V, signifying a first-order reaction kinetics, *i.e.* proportional to oxygen concentration in the alkaline electrolyte solution for the ORR. For the Tafel plots in Fig. 3c, in contrast to the large slope observed for PC(Sp/Sh)-800 (165 mV dec^{-1}) and PC(NF)-800 (96 mV dec^{-1}), the slope of HPC-800 was markedly lower at only 68 mV dec^{-1}, which was comparable to that of Pt/C (65 mV dec^{-1}), suggesting that the rate-determining step was likely the first-electron reduction process of oxygen. Note that in the low overpotential region (+0.70 to +1.00 V), the specific ORR activity of HPC-800 was determined to be the highest one in terms of kinetic current density. For example, the kinetic current density derived from the K–L plots at +0.85 V (*vs.* RHE) is 3.66 mA cm^{-2} for HPC-800. In contrast, it is only 0.21, 0.92 and 1.62 mA cm^{-2} for PC(NF)-800, PC(Sp/Sh)-800 and Pt C, respectively (Fig. 3d left part). In another comparison, we normalized the kinetic current in the kinetic-diffusion controlled region to the BET surface area of the catalysts. As shown in the right part of Fig. 3d, the HPC-800 sample exhibited a current density of 1.13×10^{-3} mA cm^{-2} at +0.85 V, again, much higher than those of PC(NF)-800 (1.47×10^{-4} mA cm^{-2}) and PC(Sp/Sh)-800 (3.62×10^{-4} mA cm^{-2}). The high kinetic currents observed in HPC-800 highlight the importance of a large specific surface in promoting ORR activity.

Long-term durability is also a major concern in catalysis science and technology. In the present study, it was evaluated by chronoamperometric measurements. As shown in Fig. S22,† after 8 h of continuous operation at +0.6 V in an O_2-saturated 0.1 M KOH aqueous solution, the commercial Pt/C electrode retained only 64.5% of its initial current density, while 86.0% retention of the initial current was observed in the HPC-800 catalyst. This difference clearly demonstrates the better durability of HPC-800 than that of commercial Pt/C.

Methanol tolerance is another critical issue that needs to be addressed in real applications. In Fig. S23,† a sudden decrease of the voltammetric current was observed on the Pt/C electrode (black curve) when 3 M methanol was injected into the electrolyte solution. Interestingly, the HPC-800 electrode nearly maintained the same ORR current (red curve) after the injection of methanol, indicative of high selectivity for the ORR. Resistance to CO poisoning is also important to fuel cell catalysts. As shown in Fig. S24,† when CO gas was injected into O_2-saturated 0.1 M KOH solution, the Pt/C electrode exhibited a gradually decrease of the ORR current and retained only *ca.* 82% of its original value after *ca.* 800 s, whereas an almost invariable current density was observed for HPC-800, implying enhanced resistance to CO poisoning as compared to Pt/C.

As an illustrating example to evaluate the performance of such catalysts in actual energy conversion devices, the HPC-800 was deposited on a Teflon-coated carbon fiber paper and utilized as the cathode for a Zn–air battery, with a Zn foil as the anode (Fig. 4a). For comparison, commercial Pt/C catalysts were also tested under the same conditions. As shown in Fig. 4b, an open-circuit voltage of 1.50 V was observed for the battery using HPC-800 as the air cathode, which was slightly higher than that observed with Pt/C (1.47 V). From the galvanostatic discharge curves, one can see that the discharge potentials for the Zn–air battery using HPC-800 as the air cathode are also superior to those with Pt/C at various current densities. Note that the discharge potentials at a current density of 1 mA cm^{-2} and 10 mA cm^{-2} with the HPC-800 air cathode are even higher than the results of a number of porous carbon catalysts reported in the recent literature (Table S3†). Even at a high current density of 100 mA cm^{-2}, the HPC-800 air cathode still displayed a discharge potential of 0.94 V, while only 0.89 V was observed for the Pt/C air cathode, indicating that the multiple hierarchical pore structures of HPC-800 indeed enhanced mass transfer for high-power output. In the galvanostatic discharge curves (Fig. 4c), no obvious decrease of voltage was observed for HPC-800 in long-term discharge until the Zn anode was completely consumed. When normalized to the mass of Zn consumed, the specific capacity of the Zn–air battery integrated with a HPC-800 air cathode was calculated to be 647 mA h g^{-1} at 10 mA cm^{-2} and 617 mA h g^{-1} at 100 mA cm^{-2}, corresponding

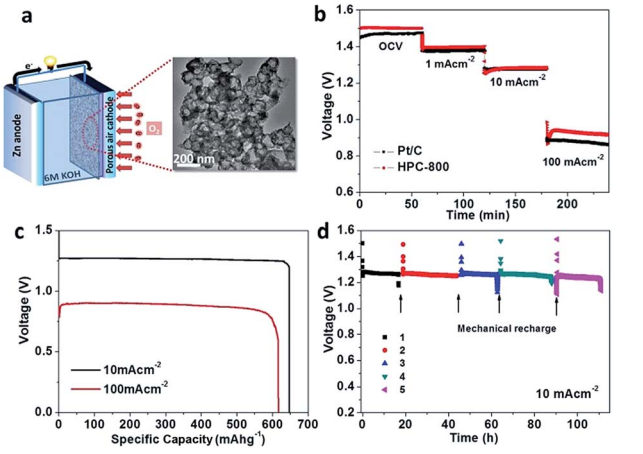

Fig. 4 (a) Schematic diagram of a primary Zn–air battery. (b) Typical galvanostatic discharge curves of Zn–air batteries with HPC-800 and Pt/C as cathode catalysts at various current densities (1, 10, and 100 mA cm^{-2}), (c) long-time galvanostatic discharge curves of a Zn–air battery using HPC-800 as the cathode catalyst. The specific capacity was normalized to the mass of consumed Zn. (d) 'Recharging' the Zn–air battery using HPC-800 as the cathode catalyst by refilling the Zn anode and electrolyte. The electrolyte for the Zn–air cell was 6.0 M KOH. Catalyst loading was 2.0 mg cm^{-2} for HPC-800 and 1.0 mg cm^{-2} for Pt/C.

to a gravimetric energy density of 834 W h kg^{-1} and 580 W h kg^{-1}, respectively. These are highly comparable to, or even better than, those of Zn–air batteries reported recently that used a nitrogen-doped porous carbon catalyst (630 mA h g^{-1} at 10 mA cm^{-2})[25] or a metal oxides catalyst (570 mA h g^{-1} at 10 mA cm^{-2})[52] as the air cathode. Importantly, after discharging, the battery could be regenerated by refueling the Zn anode and the electrolyte. In such a way, the HPC-800 air electrode worked robustly for more than 110 h with only a negligible loss of voltage (Fig. 4d), highlighting the high stability of the HPC-800 catalyst again.

Conclusions

In summary, we have developed a facile and scalable interfacially confined polymerization approach for the fabrication of two-dimensional polypyrrole nanosheets using $FeCl_3$ as both the polymerization initiator and dopants, which were then used as a precursor for the pyrolytic synthesis of nitrogen-doped carbons that contained rich nitrogen dopants and exhibited a honeycomb-like structure comprising abundant hierarchical macro/mesopores. During the carbonization process, the amorphous Fe-containing compounds in polypyrrole nanosheets evolved into nanoparticles that were distributed homogenously within the polymer matrices. These *in situ* grown nanoparticles served as volatilizable sacrificial templates to generate numerous macro/mesopores in the resulting carbons through the gradual formation of volatile Fe-containing species. XPS measurements confirmed that the resulting honeycomb-like porous carbons were co-doped with N and trace amounts of Fe. Electrochemical analysis revealed that N-doped HPCs showed apparent ORR activity in an alkaline electrolyte with the samples prepared at a pyrolysis temperature of 800 °C (HPC-800) being the best ORR catalysts among the series. In terms of onset potential, the number of electrons transferred, specific activity, durability, tolerance against methanol crossover and resistance to CO poisoning, the HPC-800 sample was found to exhibit even better ORR activity than commercial Pt/C catalysts. The efficient ORR activity of HPC-800 was primarily ascribed to the high content of N dopants and the high surface area derived from the abundant hierarchical macro- and mesopores. When used as an air cathode in a Zn–air battery, the HPC-800 catalyst even outperformed state-of-the-art Pt/C catalysts. These results highlight the unique significance of structural engineering of carbonaceous precursors based on interfacially confined polymerization in the preparation of highly efficient porous carbon catalysts for the ORR in electrochemical energy conversion devices.

Acknowledgements

This work was supported by the National Recruitment Program of Global Experts and the National Natural Science Foundation of China (NSFC 21528301 and NSFC 51402111). L. G. L. also acknowledges financial support from the Scientific Research Funds for Returned Overseas Chinese Scholars, State Education Ministry, and the Fundamental Research Funds for the Central Universities (SCUT grant no. 201522105). S. W. C. acknowledges the National Science Foundation for partial support of the work (CHE-1265635 and DMR-1409396).

Notes and references

1 M. K. Debe, *Nature*, 2012, **486**, 43–51.
2 R. Borup, J. Meyers, B. Pivovar, Y. S. Kim, R. Mukundan, N. Garland, D. Myers, M. Wilson, F. Garzon, D. Wood, P. Zelenay, K. More, K. Stroh, T. Zawodzinski, J. Boncella, J. E. McGrath, M. Inaba, K. Miyatake, M. Hori, K. Ota, Z. Ogumi, S. Miyata, A. Nishikata, Z. Siroma, Y. Uchimoto, K. Yasuda, K. I. Kimijima and N. Iwashita, *Chem. Rev.*, 2007, **107**, 3904–3951.
3 Z. H. Wen, S. Q. Ci, F. Zhang, X. L. Feng, S. M. Cui, S. Mao, S. L. Luo, Z. He and J. H. Chen, *Adv. Mater.*, 2012, **24**, 1399–1404.
4 P. P. Su, H. Xiao, J. Zhao, Y. Yao, Z. G. Shao, C. Li and Q. H. Yang, *Chem. Sci.*, 2013, **4**, 2941–2946.
5 S. I. Choi, M. H. Shao, N. Lu, A. Ruditskiy, H. C. Peng, J. Park, S. Guerrero, J. G. Wang, M. J. Kim and Y. N. Xia, *ACS Nano*, 2014, **8**, 10363–10371.
6 J. W. Hong, S. W. Kang, B. S. Choi, D. Kim, S. B. Lee and S. W. Han, *ACS Nano*, 2012, **6**, 2410–2419.
7 X. J. Liu, C. H. Cui, H. H. Li, Y. Lei, T. T. Zhuang, M. Sun, M. N. Arshad, H. A. Albar, T. R. Sobahi and S. H. Yu, *Chem. Sci.*, 2015, **6**, 3038–3043.
8 I. Katsounaros, S. Cherevko, A. R. Zeradjanin and K. J. J. Mayrhofer, *Angew. Chem., Int. Ed.*, 2014, **53**, 102–121.
9 F. Jaouen, E. Proietti, M. Lefevre, R. Chenitz, J. P. Dodelet, G. Wu, H. T. Chung, C. M. Johnston and P. Zelenay, *Energy Environ. Sci.*, 2011, **4**, 114–130.
10 Z. W. Chen, D. Higgins, A. P. Yu, L. Zhang and J. J. Zhang, *Energy Environ. Sci.*, 2011, **4**, 3167–3192.
11 R. Bashyam and P. Zelenay, *Nature*, 2006, **443**, 63–66.
12 G. Wu, K. L. More, C. M. Johnston and P. Zelenay, *Science*, 2011, **332**, 443–447.
13 H. T. Chung, J. H. Won and P. Zelenay, *Nat. Commun.*, 2013, **4**, 1922.
14 M. Lefèvre, J. P. Dodelet and P. Bertrand, *J. Phys. Chem. B*, 2002, **106**, 8705–8713.
15 E. Proietti, F. Jaouen, M. Lefevre, N. Larouche, J. Tian, J. Herranz and J. P. Dodelet, *Nat. Commun.*, 2011, **2**, 416.
16 Y. G. Li, W. Zhou, H. L. Wang, L. M. Xie, Y. Y. Liang, F. Wei, J. C. Idrobo, S. J. Pennycook and H. J. Dai, *Nat. Nanotechnol.*, 2012, **7**, 394–400.
17 B. Winther-Jensen, O. Winther-Jensen, M. Forsyth and D. R. MacFarlane, *Science*, 2008, **321**, 671–674.
18 F. Y. Cheng, J. A. Shen, B. Peng, Y. D. Pan, Z. L. Tao and J. Chen, *Nat. Chem.*, 2011, **3**, 79–84.
19 Y. Y. Liang, Y. G. Li, H. L. Wang, J. G. Zhou, J. Wang, T. Regier and H. J. Dai, *Nat. Mater.*, 2011, **10**, 780–786.
20 J. Suntivich, H. A. Gasteiger, N. Yabuuchi, H. Nakanishi, J. B. Goodenough and Y. Shao-Horn, *Nat. Chem.*, 2011, **3**, 546.
21 L. T. Qu, Y. Liu, J. B. Baek and L. M. Dai, *ACS Nano*, 2010, **4**, 1321–1326.

22 C. H. Choi, S. H. Park and S. I. Woo, *ACS Nano*, 2012, **6**, 7084–7091.
23 M. J. Zhong, S. Y. Jiang, Y. F. Tang, E. Gottlieb, E. K. Kim, A. Star, K. Matyjaszewski and T. Kowalewski, *Chem. Sci.*, 2014, **5**, 3315–3319.
24 P. Adelhelm, Y. S. Hu, L. Chuenchom, M. Antonietti, B. M. Smarsly and J. Maier, *Adv. Mater.*, 2007, **19**, 4012–4017.
25 H. W. Liang, X. D. Zhuang, S. Brüller, X. L. Feng and K. Müllen, *Nat. Commun.*, 2014, **5**, 4973.
26 R. Silva, D. Voiry, M. Chhowalla and T. Asefa, *J. Am. Chem. Soc.*, 2013, **135**, 7823–7826.
27 C. D. Liang, Z. J. Li and S. Dai, *Angew. Chem., Int. Ed.*, 2008, **47**, 3696–3717.
28 W. H. Niu, L. G. Li, X. J. Liu, N. Wang, J. Liu, W. J. Zhou, Z. H. Tang and S. W. Chen, *J. Am. Chem. Soc.*, 2015, **137**, 5555–5562.
29 W. H. Niu, L. G. Li, J. Liu, N. Wang, W. Li, Z. H. Tang, W. J. Zhou and S. W. Chen, *Small*, 2016, **12**, 1900–1908.
30 S. A. Waghuley, S. M. Yenorkar, S. S. Yawale and S. P. Yawale, *Sens. Actuators, B*, 2008, **128**, 366–373.
31 X. M. Yang and Y. Lu, *Polymer*, 2005, **46**, 5324–5328.
32 H. Y. Mi, X. G. Zhang, Y. L. Xu and F. Xiao, *Appl. Surf. Sci.*, 2010, **256**, 2284–2288.
33 Z. L. Li, M. Jaroniec, P. Papakonstantinou, J. M. Tobin, U. Vohrer, S. Kumar, G. Attard and J. D. Holmes, *Chem. Mater.*, 2007, **19**, 3349–3354.
34 J. N. Wang, L. Zhang, J. J. Niu, F. Yu, Z. M. Sheng, Y. Z. Zhao, H. Chang and C. Pak, *Chem. Mater.*, 2007, **19**, 453–459.
35 W. J. Liu, K. Tian, Y. R. He, H. Jiang and H. Q. Yu, *Environ. Sci. Technol.*, 2014, **48**, 13951–13959.
36 J. Liang, X. Du, C. Gibson, X. W. Du and S. Z. Qiao, *Adv. Mater.*, 2013, **25**, 6226–6231.
37 Z.-S. Wu, L. Chen, J. Liu, K. Parvez, H. Liang, J. Shu, H. Sachdev, R. Graf, X. Feng and K. Müllen, *Adv. Mater.*, 2014, **26**, 1450.
38 R. L. Liu, D. Q. Wu, X. L. Feng and K. Mullen, *Angew. Chem., Int. Ed.*, 2010, **49**, 2565–2569.
39 L. Lin, Q. Zhu and A. W. Xu, *J. Am. Chem. Soc.*, 2014, **136**, 11027–11033.
40 H. Kim, K. Lee, S. I. Woo and Y. Jung, *Phys. Chem. Chem. Phys.*, 2011, **13**, 17505–17510.
41 D. Deng, X. Pan, L. Yu, Y. Cui, Y. Jiang, J. Qi, W.-X. Li, Q. Fu, X. Ma, Q. Xue, G. Sun and X. Bao, *Chem. Mater.*, 2011, **23**, 1188–1193.
42 J. S. Lee, G. S. Park, S. T. Kim, M. L. Liu and J. Cho, *Angew. Chem., Int. Ed.*, 2013, **52**, 1026–1030.
43 H. R. Byon, J. Suntivich and Y. Shao-Horn, *Chem. Mater.*, 2011, **23**, 3421–3428.
44 V. Nallathambi, J. W. Lee, S. P. Kumaraguru, G. Wu and B. N. Popov, *J. Power Sources*, 2008, **183**, 34–42.
45 P. H. Matter, E. Wang, M. Arias, E. J. Biddinger and U. S. Ozkan, *J. Phys. Chem. B*, 2006, **110**, 18374–18384.
46 M. P. Woods, E. J. Biddinger, P. H. Matter, B. Mirkelamoglu and U. S. Ozkan, *Catal. Lett.*, 2010, **136**, 1–8.
47 V. Datsyuk, M. Kalyva, K. Papagelis, J. Parthenios, D. Tasis, A. Siokou, I. Kallitsis and C. Galiotis, *Carbon*, 2008, **46**, 833–840.
48 L. Zhang, K. Lee, C. W. B. Bezerra, J. L. Zhang and J. J. Zhang, *Electrochim. Acta*, 2009, **54**, 6631–6636.
49 C. W. B. Bezerra, L. Zhang, K. C. Lee, H. S. Liu, A. L. B. Marques, E. P. Marques, H. J. Wang and J. J. Zhang, *Electrochim. Acta*, 2008, **53**, 4937–4951.
50 U. I. Kramm, I. Herrmann-Geppert, P. Bogdanoff and S. Fiechter, *J. Phys. Chem. C*, 2011, **115**, 23417–23427.
51 U. I. Kramm, M. Lefevre, N. Larouche, D. Schmeisser and J. P. Dodelet, *J. Am. Chem. Soc.*, 2014, **136**, 978–985.
52 W. Ding, Z. Wei, S. Chen, X. Qi, T. Yang, J. Hu, D. Wang, L.-J. Wan, S. F. Alvi and L. Li, *Angew. Chem., Int. Ed.*, 2013, **52**, 11755–11759.
53 H. W. Liang, W. Wei, Z. S. Wu, X. L. Feng and K. Mullen, *J. Am. Chem. Soc.*, 2013, **135**, 16002–16005.
54 L. Tao, Q. Wang, S. Dou, Z. L. Ma, J. Huo, S. Y. Wang and L. M. Dai, *Chem. Commun.*, 2016, **52**, 2764–2767.
55 S. Dou, L. Tao, J. Huo, S. Wang and L. M. Dai, *Energy Environ. Sci.*, 2016, **9**, 1320–1326.